

XMM-Newton

Norbert Schartel*, Rosario González-Riestra, Peter Kretschmar, Marcus Kirsch, Pedro Rodríguez-Pascual, Simon Rosen, Maria Santos-Lleó†, Michael Smith, Martin Stuhlinger and Eva Verdugo-Rodrigo

Abstract The X-ray Multi-mirror Mission (XMM-Newton) provides simultaneous non-dispersive spectroscopic X-ray imaging and timing, medium resolution dispersive X-ray spectroscopy and optical/UV imaging, spectroscopy and timing.

In combination, the imaging cameras offer an effective area over the energy range from 150 eV to 12 keV of up to 2500 cm² at 1.5 keV and ~1800 cm² at 5 keV. The gratings cover an energy range from 0.4 keV to 2.2 keV with a combined effective area of up to 120 cm² at 0.8 keV.

XMM-Newton offers unique opportunities for a wide variety of sensitive X-ray observations accompanied by simultaneous optical/UV measurements. The majority of XMM-Newton's observing time is made available to the astronomical community by peer-reviewed Announcements of Opportunity.

The scientific exploitation of XMM-Newton data is aided by an observatory-class X-ray facility which provides analysis software, pipeline processing, calibration and catalogue generation. Around 380 refereed papers based on XMM-Newton data are published each year with a high fraction of papers reporting transformative scientific results.

Norbert Schartel, Peter Kretschmar, Maria Santos-Lleó and Eva Verdugo-Rodrigo
European Space Agency (ESA), European Space Astronomy Centre (ESAC), Camino Bajo del Castillo s/n, 28692, Villanueva de la Cañada, Madrid, Spain

Rosario González-Riestra, Pedro Rodríguez-Pascual, Simon Rosen and Martin Stuhlinger
Serco Gestión de Negocios S.L., ESAC, Camino Bajo del Castillo s/n, 28692, Villanueva de la Cañada, Madrid, Spain

Marcus Kirsch
ESA, European Space Operations Centre (ESOC), Robert-Bosch-Str. 5, 64293 Darmstadt, Germany

Michael Smith
Telespazio, ESAC, Camino Bajo del Castillo s/n, 28692, Villanueva de la Cañada, Madrid, Spain

* corresponding author (e-mail: Norbert.Schartel@esa.int)

† corresponding author (e-mail: Maria.Santos-Lleo@esa.int)

Keywords

XMM-Newton, Reflection Grating Spectrometers, European Photon Imaging Camera, Optical Monitor, X-ray detectors, X-ray telescopes, joint programmes, Target of Opportunity.

Introduction

The design and construction of XMM-Newton (X-ray Multi-Mirror Mission Newton, [1]) and its instruments utilized the extensive experience in observing X-ray astrophysical sources that European and United States (US) scientists accumulated during the previous few years.

The European X-ray Observatory SATellite (EXOSAT) which was operational between 1983 and 1986, was the European Space Agency's (ESA) direct predecessor to XMM-Newton. Two further large European X-ray satellite missions preceded XMM-Newton: the German-British-US ROSAT (Röntgensatellit) ([2]), operational from 1990 to 1999, and the Italian-Dutch BeppoSAX (Satellite per Astronomia a raggi X, ([3])), which was operational between 1996 and 2002.

XMM-Newton was proposed to ESA as the X-ray Multi-Mirror (XMM) astronomy mission by J.A.M. Bleeker³, A.C. Brinkman⁴, J.L. Culhane⁵, L. Koch⁶, K.A. Pounds⁷, H.W. Schnopper⁸, G. Spada⁹, B.G. Taylor¹⁰ and J. Trümper¹¹ in November 1982. An important milestone in the formulation of the scientific and technical requirements for XMM-Newton was the ESA workshop in Lyngby, Denmark in June 1985 ([4]), where in addition to the X-ray capabilities the importance of simultaneous optical/UV coverage was emphasized. Comprehensive technical development in European and US industries and institutes was necessary to fulfil the scientific requirements for XMM-Newton. Significant achievements took place, i.e., within X-ray optics development with mirror replication from super-polished gold-coated mandrels using nickel electroforming, X-ray CCD technology with the pn CCDs specifically developed for XMM-Newton and the development of X-ray reflection gratings technology.

XMM-Newton carries three X-ray telescopes. Located behind two of the telescopes are two Reflection Grating Spectrometers (RGS, ([5])) which intercept about

³ Leiden, The Netherlands

⁴ Utrecht, The Netherlands

⁵ Mullard Space Science Laboratory, United Kingdom

⁶ Saclay, France

⁷ Leicester, United Kingdom

⁸ Lyngby, Denmark

⁹ Bologna, Italy

¹⁰ ESA, The Netherlands

¹¹ Garching, Germany



Fig. 1 The XMM-Newton Flight Model spacecraft after completion of acoustic testing inside the Large European Acoustic Facility at the European Space Research and Technology Centre (ESTEC), Noordwijk, the Netherlands

half of the incident photons. The remaining photons are focused onto two MOS cameras ([6]). The third telescope focuses all light onto the pn camera ([7]). The two MOS cameras and the pn camera constitute the European Photon Imaging Camera (EPIC). The sixth instrument onboard XMM-Newton is the Optical Monitor ([8]). All six instruments normally observe simultaneously.

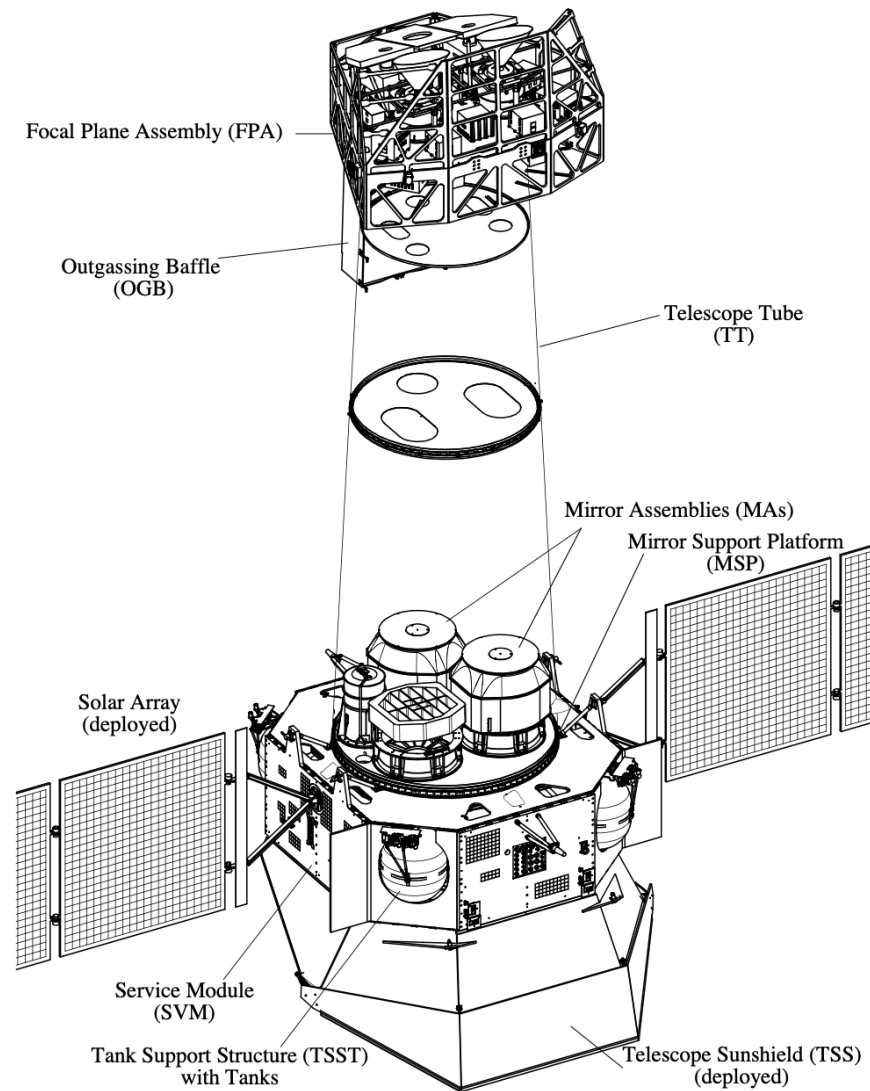


Fig. 2 A technical drawing of the XMM-Newton spacecraft from the Original Dornier Users Manual from 1999

XMM-Newton was the second cornerstone of the ESA Horizon 2000 program and was launched by an Ariane V rocket on December 10, 1999. It was ESA's first large observatory-class mission, where the scientific support (peer review proposal selection, calibration, analysis software and archive) was planned for and provided from the start.

In the following we give an overview of the spacecraft (page 5), the X-ray telescopes (page 8), and the instruments (EPIC (page 10), RGS (page 15), and OM (page 19)) as well as how the ground segment is organized (page 24), how the observing program is implemented (page 25) and how the science data can be analyzed (page 27), the observing strategy (page 29) and its evolution through the years and the scientific output as reflected, e.g., in published papers.

The Spacecraft

The three-axis stabilized, 3.8 tonne spacecraft, see Fig. 1 and Fig. 2, has a pointing accuracy of one arcsec. It consists of three main sections: a 7 m-long telescope tube between the squarish service module which houses the instruments and the telescope module accommodating the three telescopes. This gives the spacecraft a total length of 10.8 m. Its pair of solar panels have a 16 m span.

The spacecraft was built by Dornier (now Airbus Defence and Space) from 1994 to 1999. Its main subsystems are the Attitude and Orbit Control System including the Reaction Control System (AOCS and RCS), On Board Data Handling System (OBDH), the Power and Thermal Systems (EPS, TCS), and the Radio Frequency System (RF). All subsystems have their own redundancy concepts.

The AOCS provides three-axis stabilization during all modes. The AOCS architecture is formed around the Attitude Control Computer (ACC), running the software for mode control and the attitude and thrust control laws. The AOCS uses a Star Tracker and Fine Sun Sensor to provide the absolute reference. The Star Tracker is a small telescope with $3^\circ \times 4^\circ$ field of view (FOV) and a thermo-electrically cooled CCD detector. The Fine Sun Sensors deliver pitch and roll information and their FOV is $\pm 45^\circ$ per sensor. Backup sensors such as Inertial Measurement Units are also used for control in case of main sensors unavailability such as the Fine Sun Sensor during the eclipse and the Star Tracker when its FOV is blinded or the guide star is lost. Reaction wheels are the primary actuators for attitude control. In the classic three-wheel mode operations scenario, any three out of four reaction wheels are used for active control, each one with a net torque of 0.2 Nm and 40 Nms momentum capacity. The reaction wheel that is not used for active control was originally switched off and only used in cold redundancy. The failure detection and correction is performed using hardware only.

The RCS is a monopropellant propulsion system utilizing hydrazine (N_2H_4) in blow-down mode with helium as the pressurant. The propellant is stored in four surface tension tanks placed around the central cone element of the service module structure of the spacecraft. Eight monopropellant 20 Newton thrusters, divided into two redundant branches, each consisting of four thrusters, are used for delta-V maneuvers, attitude control, and reaction wheel desaturation.

The functional objective of the OBDH subsystem is to provide command and telemetry capability allowing the overall spacecraft control and to provide clock and timing facilities for the other subsystems. It consists of a CDMU, two Remote Ter-

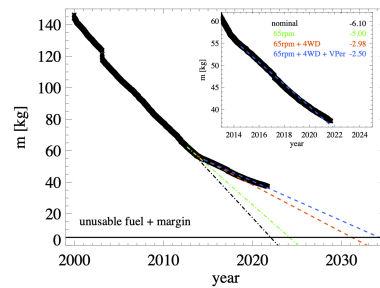


Fig. 3 XMM-Newton fuel consumption calculated via the flight dynamics book-keeping method. The extrapolation does not include any contingency cases. As of 2013 the annual fuel consumption was reduced by more than a factor of two

minimal Units (RTUs) and six Digital Bus Units (DBUs). The RTUs connect via standard discrete interfaces to all users without intelligence (i.e. microprocessors), e.g., the EPS, RF, and TCS. The RTUs handle all instrument functions and the AOCs where no microprocessor involvement of the relevant unit is available. The OBDH system is based on the implementation of the ESA Packet Telecommand Standard PSS-04-107, ESA Packet Telemetry Standard PSS-04-106 and an ESA OBDH Data Bus as main path for telecommand distribution and telemetry acquisition. The users are distinguished between Packet Terminals and Non-Packet Terminals.

The EPS provides electrical power to all subsystems. During sunlight power is provided by the fixed, two-wing deployable solar array and in eclipse by two nickel-cadmium batteries. Both energy sources are conditioned to provide a single 28 V DC regulated bus. The solar array generates a maximum power of 1.8 kW.

The TCS features a combination of active and passive thermal control systems originally without any onboard control software. This means that all the heater lines are either online controlled from ground or thermostat-controlled. The ground commands open or close transistor switches installed within the service module power distribution units, focal plane assembly power distribution units and mirror thermal control unit in the power lines between heater and latching current limiters. During ground contact outages, the heater lines are controlled by bi-metal mechanical thermostats in the satellite.

The Radio Frequency (RF) subsystem is composed of three main blocks which are two Low Gain Antennas, two transponders, and a Radio Frequency Distribution Network with two switches to connect the transponders to the antennae. An S-Band transponder comprises three main modules: a diplexer, a receiver, and a transmitter. The receiver assures the reception of signal in the range of 2025 to 2120 MHz (S-band) and the phase demodulation of the telecommand signal and the ranging tones. The transmitter performs the modulation of the telemetry video signal and the

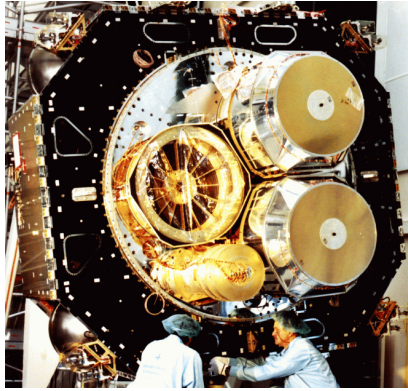


Fig. 4 The XMM-Newton mirror modules on the backside of the XMM-Newton service module. One spider is visible on the left side, while the two other modules are covered

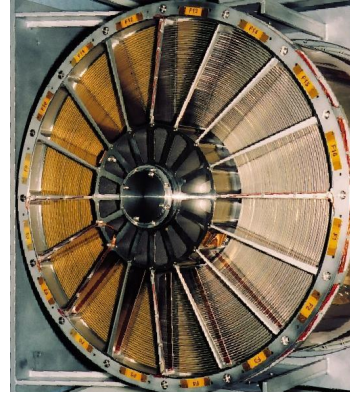


Fig. 5 One spider of the XMM-Newton mirror module carries a full set of 58 flight mirror shells

ranging tones, as well as the power amplification of the output signal. The diplexer allows simultaneous operation of the receiver and the transmitter with just a single RF connection. This configuration allows an effective data rate of 80 kb s^{-1} for the downlink and 2 kb s^{-1} for the uplink.

XMM-Newton has no onboard data storage capacity, so all data are immediately down-linked to the ground in real time. The mission requires control 24/7, 365 days per year through a live ground station connection, since the spacecraft has only limited automation.

After a loss of contact to the spacecraft for 5 days in 2008, due to one unreliable RF subsystem antenna switch, the mission was recovered and the mission operations concept revised to use both the prime and redundant transponders for communication. This method has not reduced the science return [9].

In 2013, the AOCS was re-programmed in order to also use the backup reaction wheel in a new operations scenario called "4 wheel drive" (4WD). Since 2013 the degree of freedom that was introduced by this change allows the fuel consumption to be reduced by a factor of two, see Fig. 3, and provides as well mitigation measures against a degradation effect on two of the reaction wheels [10] [11]. Technically, the observatory currently has sufficient resources to operate until 2031

The onboard software has also been updated several times to improve and streamline mission operations and to support the provision of fuel in the near depletion regime, allowing now fine thermal control of some subsystems as well as switch state protection of some Heater Power Lines [11].

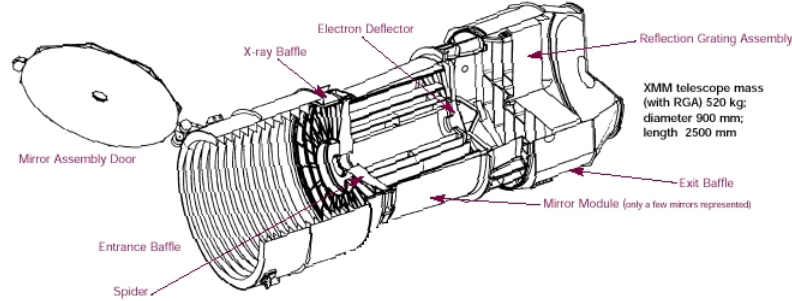


Fig. 6 X-ray telescope configuration

X-Ray Mirrors

Each of the three X-ray telescopes on board XMM-Newton consists of 58 Wolter I grazing-incidence mirrors which are nested in a coaxial and confocal configuration, see; [12], [13], [14], [1] and [15], see Fig. 4, Fig. 5, and Fig. 6. The design of the optics was driven by the requirement of obtaining the highest possible effective area over the 0.2-12.0 keV energy range, with particular emphasis in the region around 7 keV. Thus, the mirror system had to utilize a very shallow grazing angle of 30' in order to provide sufficient reflectivity at high energies. The telescopes' focal length is 7.5 m, and the diameter of the largest mirrors is 70 cm, to be compatible with the shroud of the launcher.

The mirrors were replicated from super-polished gold-coated mandrels using a nickel electroforming technique. The 58 mirrors of each telescope are bonded onto their entrance aperture to the 16 spokes of a single spider. An electron deflector is located in the exit aperture which produces a circumferential magnetic field to prevent low-energy electrons reflected by the mirrors reaching the focal plane detectors. X-ray baffles, consisting of 2 sieve plates each with 58 annular apertures, are located in front of the mirror systems. They act as collimators and considerably reduce the amount of straylight in the FOV of the focal plane cameras.

The spider is connected to the support platform via an aluminum interface structure (the MIS: Mirror Interface Structure) consisting of an outer cylinder and an interface ring. On two of the modules, the ring interfaces the mirror module to a Reflection Grating Assembly (RGA). To minimize the mechanical deformation of the mirrors and therefore the optical degradation, the flatness of the interface between the spider and the MIS is less than 5 micron.

The first critical parameter determining the quality of an X-ray mirror module is its ability to focus photons. This is one of XMM-Newton's major strengths: the core of its on-axis point-spread function (PSF) is narrow and varies little over a wide energy range (0.1-6 keV). Above 6 keV, the PSF becomes only slightly more energy dependent.

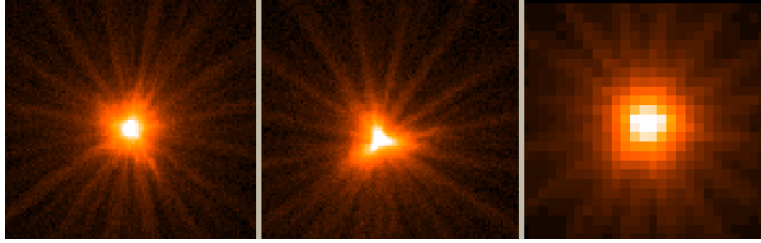


Fig. 7 On-axis point-spread function (PSF) of the EPIC-MOS1, EPIC-MOS2 and EPIC-pn X-ray telescopes (left to right) registered on the same source with each EPIC-MOS camera in Small Window mode, and the EPIC-pn camera in Large Window mode

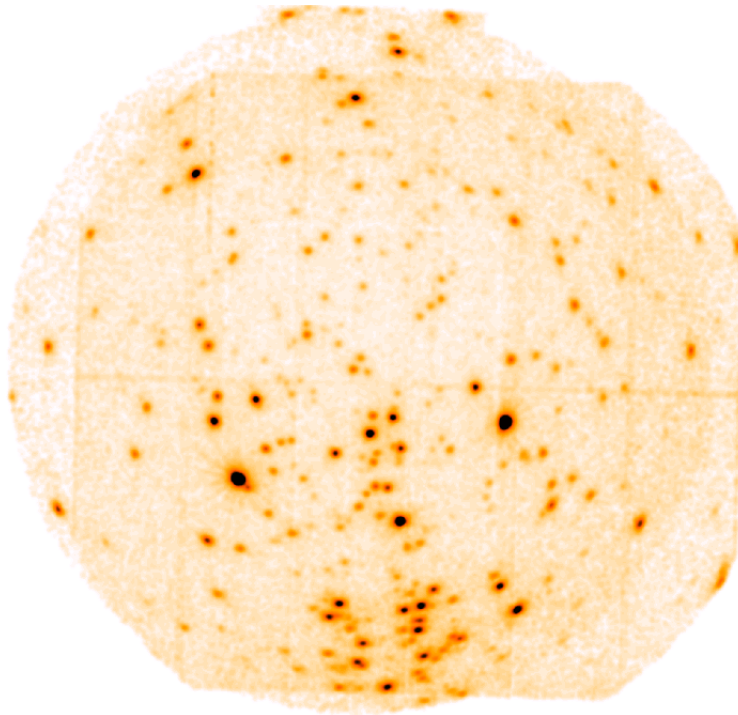


Fig. 8 The dependence of the X-ray PSF on position in the FOV. This image was made from an observation towards the Orion molecular cloud. EPIC-pn, EPIC-MOS1 and EPIC-MOS2 exposures have been merged and exposure corrected. The image has been slightly smoothed with a Gaussian of 10'' FWHM. The intensity scale is square root

The details of the PSF shapes and energy dependencies differ between the respective telescopes. As an example, Fig.7 shows the in-orbit on-axis PSF of the EPIC-MOS1, EPIC-MOS2, and EPIC-pn X-ray telescopes, measured on the same source. This figure is primarily provided to show the shape of the PSF, with e.g., the radial substructures caused by the spiders holding the mirror shells.

The PSF of the X-ray telescopes depends on the source off-axis angle, i.e., its distance from the center of the FOV. It also depends slightly on the source azimuth within the FOV. In Fig.8 the dependence of the shape of the XMM-Newton X-ray PSF on the position within the FOV is presented. The PSF at large off-axis angles is elongated due to off-axis aberration (astigmatism).

European Photon Imaging Camera (EPIC)

The European Photon Imaging Camera (EPIC) offers the possibility of performing extremely sensitive imaging observations over the telescopes' circular FOV of 30' diameter in the 0.15 - 15keV energy range with moderate spectral ($E/\Delta E \sim 20-50$) and angular resolution (6" FWHM point-spread function). One camera can be operated with a time resolution as fast as 7 μ s.

The EPIC consists of three imaging spectrometers each of which is located at the focus of one of the three coaligned X-ray telescopes. Two of the cameras consist of an array of seven EPIC-MOS-type Charge-Coupled Devices (CCDs) [6] and are located behind the X-ray telescopes which share their optical paths with the RGS [5]. The grating assemblies intercept the light path such that about 44% of the original incident flux reaches the EPIC-MOS cameras. The third EPIC camera system employs a monolithic pn-CCD array [7] and is located at the focus of an unobstructed X-ray telescope. Each EPIC instrument is fitted with an identical filter wheel containing several X-ray transmissive but optical light blocking filters as well as fully open and fully closed positions. The EPIC instrument also includes the Radiation Monitoring System, which detects the ambient electron and proton fluxes and is used as part of the warning system to protect the cameras in case of harmful radiation levels.

The Instrument

Each EPIC-MOS camera contains seven front-illuminated CCDs; see Fig. 9. These are three-phase frame transfer devices of high resistivity epitaxial silicon with an open-electrode structure. The central CCD is located at the telescope focus while the outer six CCDs are stepped towards the mirror to follow approximately the focal plane curvature to help with maintaining focus for off-axis sources. The CCD imaging area is 2.5×2.5 cm, and contains 600×600 , 40 micron square pixels; one pixel covers 1.1×1.1 " on the FOV; 15 pixels cover the mirror PSF half en-

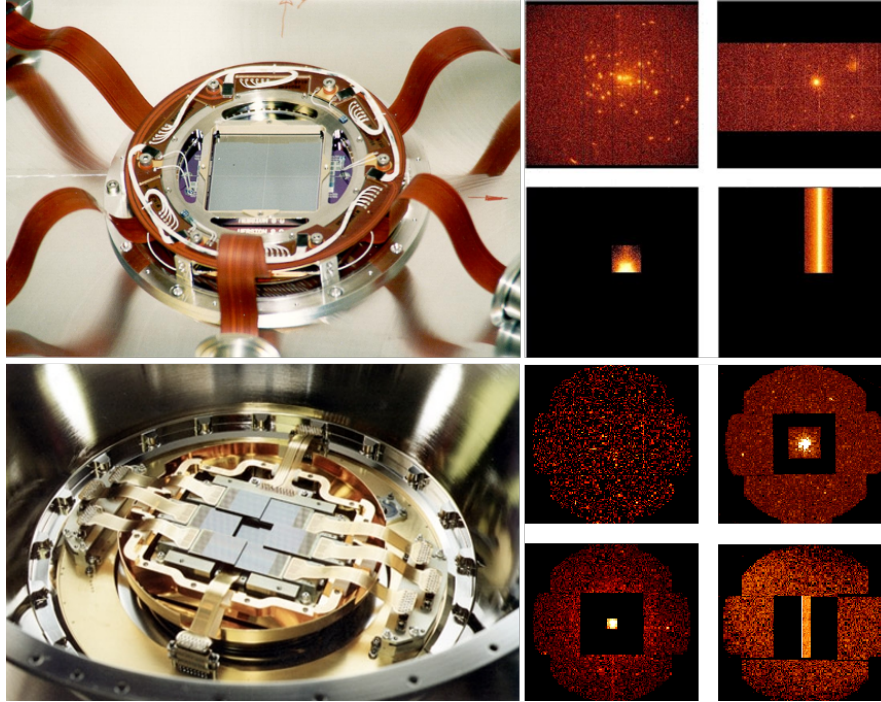


Fig. 9 Images of the CCD detectors EPIC-pn (top) and EPIC-MOS as well as examples of the FOVs using the different observation modes - Full Frame, Large Window, Small Window, and Timing

ergy width of $15''$. The mosaic of seven CCDs covers the focal plane of 62 mm, equivalent to 28.4 arcmin, in diameter. The two EPIC-MOS cameras are arranged on the spacecraft in a mutually orthogonal layout, such that the gaps in sky coverage between the outer CCDs of one unit are covered by the other.

The EPIC-pn detector was specifically designed for the XMM-Newton X-ray telescope performance in terms of angular resolution, FOV, and energy pass band. The EPIC-pn camera array consists of 12 individually operated 3×1 cm back-illuminated pn-CCDs, monolithically implanted on a single wafer; see Fig. 9. The instrument is subdivided into four individual quadrants of three pn-CCD subunits with a format of 200×64 pixels operated in parallel. The resulting imaging area of 6×6 cm covers approximately 97% of the telescope FOV; about 6 cm^2 of the CCD sensitive area lies outside the FOV and allows instrumental background studies. The CCD pixel size is 150×150 microns ($4.1''$) with a position resolution of 120 microns, resulting in an equivalent angular resolving capability for a single photon of $3.3''$. The focal point of the X-ray telescope is located on CCD 0 of quadrant 1.

Since launch, EPIC has suffered five events, ascribed to micrometeoroid impacts along the boresight, which have resulted in permanent damage to the detectors. In three cases the lasting effect was limited to the appearance of individual bright

pixels. However, two events resulted in more extensive damage: the loss of EPIC-MOS1 CCD 6 and the appearance of a hot column passing very close to the EPIC-MOS1 boresight, and the loss of EPIC-MOS1 CCD 3.

The EPIC cameras allow several data acquisition modes to accommodate a range of source fluxes and to allow for fast-timing measurements, see Fig. 9. With respect to the standard Full Frame imaging mode, the CCD readout speed can be increased at the cost of a smaller area of the window to be read out. Timing mode (and also Burst mode for EPIC-pn) allow the fastest readout cycles by sacrificing the spatial information in the readout direction. In the case of EPIC-MOS, the various modes affect the central CCD only while the six peripheral CCDs remain in standard Full Frame imaging mode. The EPIC-pn camera CCDs can be operated in common modes across all quadrants for Full Frame, Extended Full Frame and Large Window modes, or just with the single focal point CCD being read out for Small Window, Timing and Burst modes. The duty cycle efficiency of most modes is 95–100%. However, for the EPIC-pn Small Window mode and, especially, Burst mode the efficiencies are lower, at 71.0% and 3.0%, respectively. A summary of the basic characteristics of the science modes is given in Table 1.

EPIC-MOS (central CCD; pixels) [1 pixel = 1.1"]	Time resolution	Max. point source count rate (flux) [s ⁻¹] ([mCrab])
Full frame (600 × 600)	2.6 s	0.50 (0.17)
Large window (300 × 300)	0.9 s	1.5 (0.49)
Small window (100 × 100)	0.3 s	4.5 (1.53)
Timing uncompressed (100 × 600)	1.75 ms	100 (35)
EPIC-pn (array or 1 CCD; pixels) [1 pixel = 4.1"]	Time resolution	Max. point source count rate (flux) [s ⁻¹] ([mCrab])
Full frame (376 × 384)	73.4 ms	2 (0.23)
Extended full frame (376 × 384)	199.1 ms	0.7 (0.09)
Large window (198 × 384)	47.7 ms	3 (0.35)
Small window (63 × 64)	5.7 ms	25 (3.25)
Timing (64 × 200)	0.03 ms	800 (85)
Burst (64 × 180)	7 μs	60,000 (6300)

Table 1 Summary of the basic characteristics of the EPIC science modes.

As the EPIC detectors are not only sensitive to X-ray photons but also to visible and UV light, the cameras include aluminized optical blocking filters. Their design is a compromise between the need to prevent optical and UV photons from reaching the CCD plane, and the need to absorb as few X-ray photons as possible, especially at the lowest X-ray energies. There are four filters in each EPIC camera. Two are thin filters made of 1600 Å of unsupported polyimide film with a single 400 Å layer of aluminum evaporated on one side. A medium filter is of similar construction but with an 800 Å layer of deposited aluminum. The thick filter is constructed on an unsupported 3300 Å thick polypropylene film with 1100 Å of aluminum and 450 Å

of tin evaporated on the film to block the UV that would otherwise be transmitted by the polypropylene. The filters are self-supporting and 76 mm in diameter. Two additional positions on the filter wheel are occupied by the closed (1.05 mm of aluminum) and open positions, respectively. The former is used to protect the CCDs from soft protons, while the open position could in principle be used for observations where the light flux is very low and no filter is needed; see Fig. 10.

Scientific Performance

The overall EPIC-MOS quantum efficiency (QE) is smooth function with prominent features at the Si and O edges. The low-energy QE varies somewhat from CCD to CCD. It has become apparent that over the course of the mission the response of the EPIC-MOS cameras (primarily EPIC-MOS2) is deteriorating below ~ 1 keV. It is suspected that this is due to a steady buildup of contaminant which has adhered to the surface of the cameras, absorbing a fraction of the incoming photons. This development is being closely monitored and the time-dependent change in efficiency is included in the instrument calibration. The low-energy redistribution function (RMF) of the EPIC-MOS CCDs has a complex shape consisting of a main photo peak combined with a low-energy shoulder, the latter becoming dominant towards the very lowest energies. In-flight measurements show it to be both temporally and spatially dependent, with the most pronounced effects around the bore-sight location. The energy resolution of the EPIC-MOS cameras showed a significant temporal degradation in the early stage of the mission. However, in November 2002 the cameras were cooled to run at a lower operating temperature, thus significantly restoring the energy resolution and reducing its subsequent rate of degradation.

The EPIC-pn QE low-energy response is limited by the radiation entrance window and properties of the Si L-edge, whereas the high-energy response is determined by the fully depleted $300 \mu\text{m}$ depth of silicon. Further prominent features are due to absorption in the SiO_2 passivation layer (at 528 eV) and the X-ray absorption fine structure around the Si K-edge (at 1.838 keV). The absolute QE was calibrated on ground at synchrotron facilities under conditions comparable to space operations, and further in-flight calibration measurements have shown it to be very stable over the course of the mission. In-flight measurements of the energy resolution show a steady degradation by about 2.5 eV/year at 6 keV for Full Frame mode data at the boresight location.

The XMM-Newton observatory, by virtue of its large FOV and high throughput, provides good capabilities for the detection of low surface brightness emission features from extended and diffuse galactic and extragalactic sources. In order to fully exploit this, an understanding of the background is required. There are several different components to the EPIC background:

- Astrophysical background which is dominated by thermal emission at energies below 1 keV and a power-law at higher energies (primarily from unresolved cos-

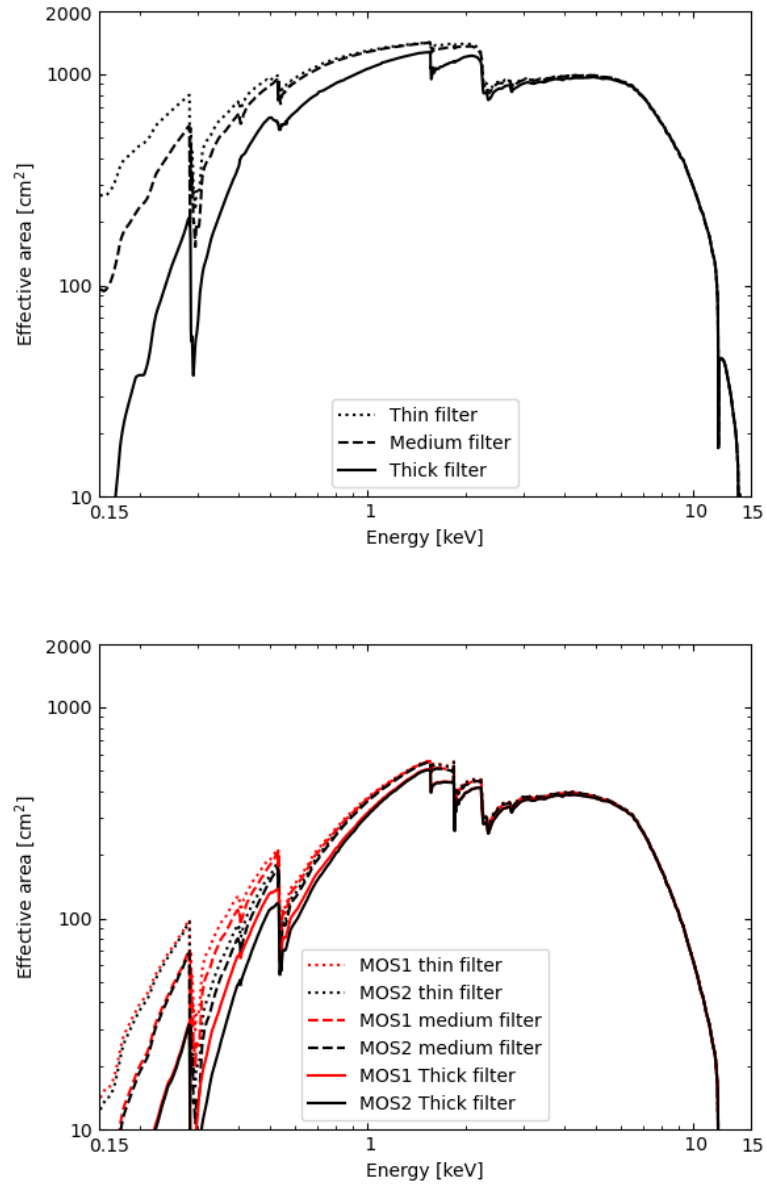


Fig. 10 Current total effective areas of the EPIC-pn (top) and EPIC-MOS (bottom). Due to contamination, probably by hydrocarbons, the EPIC-MOS2 effective area has decreased slightly at lower energies over the mission duration compared to the EPIC-MOS1

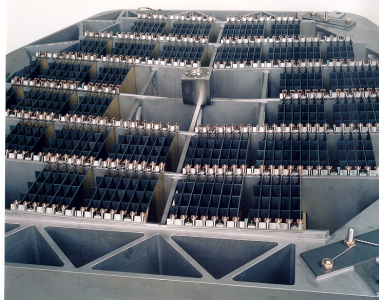


Fig. 11 View of one of the Reflection Grating Arrays

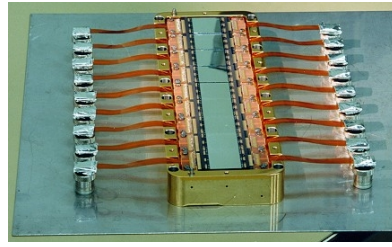


Fig. 12 View of one of the CCD benches

mological sources) and sometimes a contribution from solar wind charge exchange. This background varies over the sky at lower energies.

- Particle background, consisting of soft proton flares (with spectral variations from flare to flare) and that induced by cosmic rays, both directly by particles penetrating the CCDs and indirectly by fluorescence of instrument and spacecraft materials.
- Electronic noise consisting of CCD readout noise (mainly below 200 eV) and effects of detector defects such as bad pixels.

As part of the EPIC instrument, the EPIC Radiation Monitor (ERM) experiment registers the total count rate and basic spectral information of the background radiation impinging on the spacecraft. Its main purpose is to supply particle environment information for the safe and correct operation of the EPIC cameras.

The Reflection Grating Spectrometers (RGSs)

In two of the three XMM-Newton X-ray telescopes (those having EPIC-MOS cameras), about half of the X-ray light is utilized by the RGSs. A detailed description of the instrument is given in [5].

The spectral range covered by the RGS of 5-38 Å has a high density of emission lines including the K-shell transitions and He-like triplets of light elements, such as C, N, O, Ne, Mg, and Si as well as the L-shell transitions of heavier elements such as Fe and Ni, thus offering a large number of diagnostic tools to investigate the physical conditions and chemical composition of the emitting material.

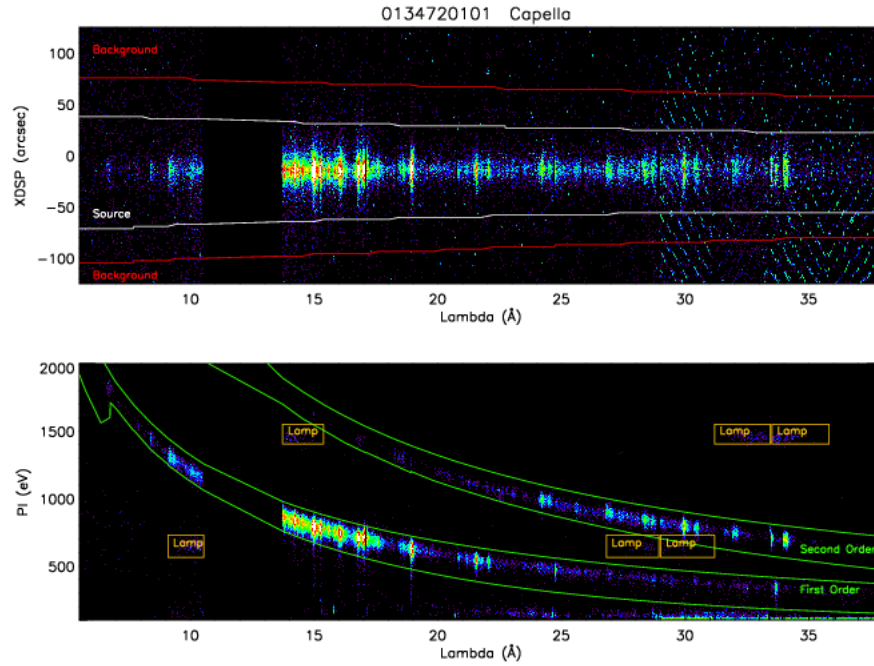


Fig. 13 RGS data for an observation of Capella. The dispersion axis runs horizontally and increases to the right. The top panel shows the image of the dispersed light in the detector. The cross dispersion is along the vertical axis. The bottom panel shows the order selection plane, with the energy (PI), on the ordinate. This also illustrates the mechanism used for separation of first, second and higher grating orders. Standard data extraction regions are indicated by the curves

The Instrument

Each RGS consists of an array of reflection gratings which diffract X-rays to an array of nine dedicated Charge-Coupled Devices (CCDs), located along the spectrograph Rowland circle. Both spectrometers cover the same FOV, with the dispersion direction along the spacecraft Z-axis. The size of the FOV in the cross-dispersion direction is $5'$. In the dispersion direction, the aperture of RGS covers the entire FOV of the mirrors, although the effective area decreases significantly for off-axis sources. Each instrument consists of two identical chains with the following units:

- The Reflection Grating Array unit (RGA); see Fig. 11.
- The Focal Plane Camera unit (RFC), including the detectors and the front-end electronics; see; Fig. 12.
- The Analogue Electronic units (RAE) that process data and control the readout sequence of the CCDs.
- Two Digital Electronic units (RDE) that control the instrument.

The RGAs consist of an array of reflection gratings (182 for RGS1, 181 for RGS2). Each RGA intercepts 58% of the total light focused by the mirror module. The grating plates have mean groove densities of about $645.6 \text{ lines mm}^{-1}$. The dispersion of the instrument is a slowly varying function of dispersion angle, approximately 8.3 and 12.7 mm \AA^{-1} at 15 \AA in first and second order, respectively.

The dispersion equation for the spectrometer is given by:

$$m \lambda = d (\cos \beta - \cos \alpha) \quad (1)$$

where m is the spectral order (-1, -2...), d is the groove spacing, β is the angle between the outgoing ray and the grating plane, and α is the angle between the incoming ray and the grating plane. The light is primarily diffracted into the "inside" spectral orders, where $m < 0$, so that $\beta > \alpha$.

The RGA diffracts the X-rays to an array of nine MOS back-illuminated CCDs. Each has 1024×768 pixels, half exposed to the sky and half used as a storage area. During readout, 3×3 pixel on-chip binning is performed, leading to a bin size of $(81 \mu\text{m})^2$, which is sufficient to fully sample the line spread function, reducing the readout time and the readout noise. In the dispersion direction one bin corresponds to about 7, 10, and 14 mÅ in first order and about 4, 6, and 10 mÅ in second order for wavelengths of 5, 15 and 38 Å, respectively. The size of one bin projected onto the sky is about 2.5" in the cross-dispersion direction and roughly 3, 5 and 7" and 4, 6, and 9" in the dispersion direction at 5, 15 and 38 Å in first and second order, respectively.

After the first week of operations, an electronic component in the clock driver of CCD4 in RGS2 failed, affecting the wavelength range from 20.0 to 24.1 Å. A similar problem occurred in early September 2000 with CCD7 of RGS1 covering 10.6 to 13.8 Å. The total effective area is thus reduced by a factor of two in these wavelength bands (see Fig. 14).

In 2007, the readout method in RGS2 was changed from double-node, in which data from the two halves of the chips are retrieved separately, to single-node, in which data from the whole chip are read out through a single amplifier. Hence, RGS2 frame times are twice as long as those from RGS1.

The standard mode of operation of the RGS instrument is called "Spectroscopy". It consists of a two-dimensional readout of one or more CCDs over the full energy range. The accumulation time when reading the eight functional CCDs is 4.8 s for RGS1 and 9.6 s for RGS2.

To mitigate the effects of pile-up, very bright sources can be observed in the RGS "Small Window" mode. In this mode, only the central 32 of the 128 CCD rows in the cross-dispersion direction are read. The CCD readout time is therefore decreased by a factor 4 compared to Spectroscopy mode. It can be further decreased by reading only a subset of the CCDs.

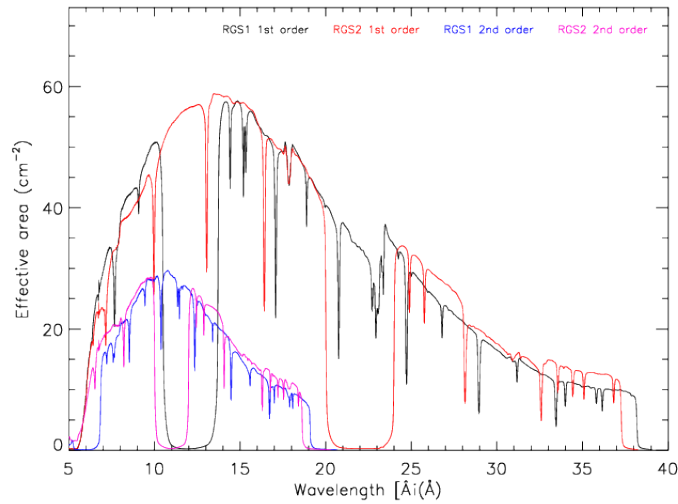


Fig. 14 Example of the RGS effective area for a recent observation. Clearly visible are the gaps due to the non-working CCDs and, in RGS1, the prominent instrumental O edge near 23 Å

Scientific Performance

A consequence of the diffraction equation (1) is that orders overlap on the CCD detectors of the RFC. Separation of the spectral orders is achieved by using the intrinsic energy resolution of the CCDs, which is about 160 eV FWHM at 2 keV. The dispersion of a spectrum on an RFC array is shown in the bottom panel of Fig. 13. First and second orders are very prominent and are clearly separated in the vertical direction (i.e., in CCD energy, or PI, space). Photons of higher orders are also visible for brighter sources. The calibration sources can also be seen in the bottom panel as short horizontal features (Fig. 13).

A summary of the RGSs' performance is given in Tab 2. A complete overview of the performance of the RGS, instrumental details and calibration procedures can be found in [16].

The calibration of the RGS effective area is based on a combination of ground measurements and in-flight observations (Fig. 14). Empirical corrections have been introduced along the years, the first one based on the assumed power law form of blazar spectra, followed by the recognition of wavelength-dependent sensitivity changes consistent with a buildup of hydrocarbon contamination on the CCD surface. There are indications of a continuous decrease in effective area over the

		RGS1			RGS2		
		10 Å	15 Å	35 Å	10 Å	15 Å	35 Å
Effective area (cm ²)	1 st order	51	61	21	53	68	25
	2 nd order	29	15	–	31	19	–
Resolution (km s ⁻¹)	1 st order	1700	1200	600	1900	1400	700
	2 nd order	1000	700	–	1200	800	–
Wavelength range	1 st order	5 – 38 Å (0.35 – 2.5 keV)					
	2 nd order	5 – 20 Å (0.62 – 2.5 keV)					
Wavelength accuracy	1 st order	±5 mÅ			±6 mÅ		
	2 nd order	±5 mÅ			±5 mÅ		

Table 2 RGS In-orbit Performance

last years, in both instruments and affecting most of the spectral range. This decrease cannot be explained by only contamination by hydrocarbons. Its origin is not understood. This calibration takes into account this effect, following an empirical algorithm. The first-order effective area peaks around 15 Å (0.83 keV) at about 120 cm² for the two spectrometers.

The wavelength scale is determined by the geometry of the various instrument components. The original pre-flight calibration kept the wavelength scale accuracy well within specification. Nevertheless, it has been improved by taking into account some systematic effects. With these corrections, the accuracy of the wavelength scale is now of order of 6 mÅ.

The observed line shape is well represented by the model. The empirically determined width of strong emission lines is a slowly varying function of wavelength in both instruments, with a mean FWHM of about 70 mÅ in first order and 50 mÅ in second order, giving a spectral resolution that increases with wavelength. It is estimated that an observed line broadening of more than 10% of the FWHM can be considered to be significant for strong lines.

The current status of the instruments and the calibration can be found in the "XMM-Newton Users Handbook" ([15]) and in the document "Status of the RGS Calibration" [17], both available at the XMM-Newton website.

Optical Monitor (OM)

The Optical Monitor (OM) provides simultaneous optical/UV coverage of sources in the EPIC field of view, extending the wavelength range of the mission and enhancing its scientific return.

The photon-counting nature of the instrument and the low in-space background mean it is highly sensitive for the detection of faint sources, despite its small size, being able to reach about magnitude 22 (5 σ detection) in the B filter in 5 ks of exposure (with maximum depth in the White filter). The provision of UV and optical

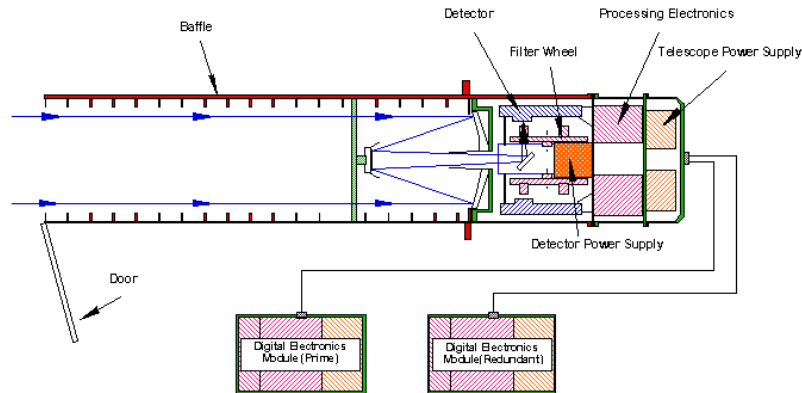


Fig. 15 Schematic of the Optical Monitor

grisms permits low-resolution spectroscopic analyses, while the fast mode timing options allow detailed studies of temporal variability.

The Instrument

The OM is a 2 m-long, 30 cm diameter telescope of Ritchey-Chretien design, with a focal length of 3.8 m (f/12.7). After passing through the primary mirror hole, the light beam impinges on a rotatable 45° flat that deflects it to one of two redundant detector chains. Each chain comprises a filter wheel containing 11 apertures (V (500-600 nm), B (380-500 nm), U (300-400 nm), UVW1 (220-400 nm), UVM2 (200-280 nm), UVW2 (180-260 nm) and White-light (180-700 nm) broadband filters, visible (290-600 nm) and UV (180-360 nm) grisms for dispersive (resolving power $(\lambda/\Delta\lambda) \sim 180$) spectroscopy, a magnifier¹², and a mirror acting as a blocking filter). A schematic of the OM is shown in Fig. 15, while the photographs in Figs. 16 and 17 show the telescope and the filter wheel assembly, respectively.

The detector, located behind the filter wheel in each chain, is a Micro Channel Plate (MCP)-intensified CCD (MIC), comprising a S20 photocathode, a pair of MCPs, a P-46 phosphor, a fiber taper and a CCD. An electron liberated from the photocathode by an incident sky photon drifts to the upper MCP where a potential accelerates it along a pore, creating a cascade of electrons by collisions with the pore walls. On passing through the second MCP, this charge cloud is amplified to around $5 \times 10^5 - 10^6$ electrons, and these impinge on the phosphor, resulting in a burst of photons. This photon burst, spatially localized by the MCP arrangement,

¹² not available for use

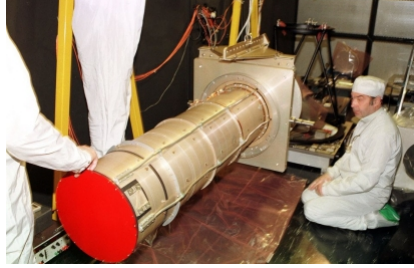


Fig. 16 The Optical Monitor at Mullard Space Science Laboratory, UK

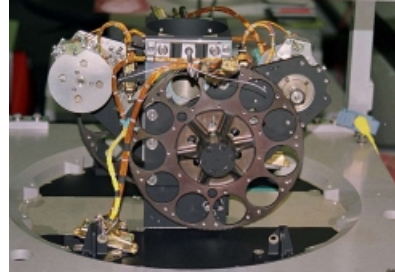


Fig. 17 One of the two filter wheels positioned in front of the OM's CCD detectors

then traverses the fibre taper, onto the CCD, which has 256×256 light-facing pixels (each 4×4 arcsecs on the sky). The footprint of the photon burst at the CCD covers about 3×3 CCD pixels. On readout, an onboard algorithm then centroids each footprint to $1/8$ of a CCD pixel, creating an effective image of 2048×2048 image pixels (maximum resolution, 0.5×0.5 arcsec pixels on the sky). The CCD is read out about 90 times (frames)/s (for the full field). Thus, each sky photon incident on the photocathode that yields a footprint at the CCD within the frame is subject to onboard validation thresholds, recorded as an incident event by the onboard data processing system.

The OM has two main modes of operation: Imaging mode, where events from each frame are accumulated into a single image covering the total exposure time, and Fast mode, where, for a small $11'' \times 11''$ window, each event is time-tagged, yielding an event stream. In Imaging mode, the observer has, subject to telemetry-related constraints, significant freedom to define window(s) for optimum sky coverage for their science goals. This may involve coverage of the whole field, at the expense of longer instrument overheads, or coverage of more localized areas of the field via up to five smaller windows. Grism data is taken either in a Full-field mode, potentially yielding spectra from all sufficiently bright objects in the field, or with a narrow, predefined window, designed to concentrate on a specific target observed at the boresight. In Fast mode only two Fast mode windows are allowed, though normally these can be used in conjunction with image mode windows. The highest time resolution in fast mode is 0.5 s.

Three important consequences of the OM design on its output data are as follows: (1) When two or more photon bursts arrive at the CCD within the same readout frame and their footprints spatially overlap, the probability of which increases with source count rate and/or longer frame times, they may not be distinguished and so be recorded as a single event. This effect is referred to as coincidence loss and is similar to the pile-up effect in the EPIC cameras. (2) The instrument design, particularly the fiber taper, results in a distortion of the imaged field compared to the real sky. (3) For speed, the onboard algorithm exploits a lookup table to centroid the count distribution in each 3×3 CCD-pixel footprint, a simplification that results in a so-called “modulo-8” pattern appearing on a scale of 8 pixels in the 2048×2048

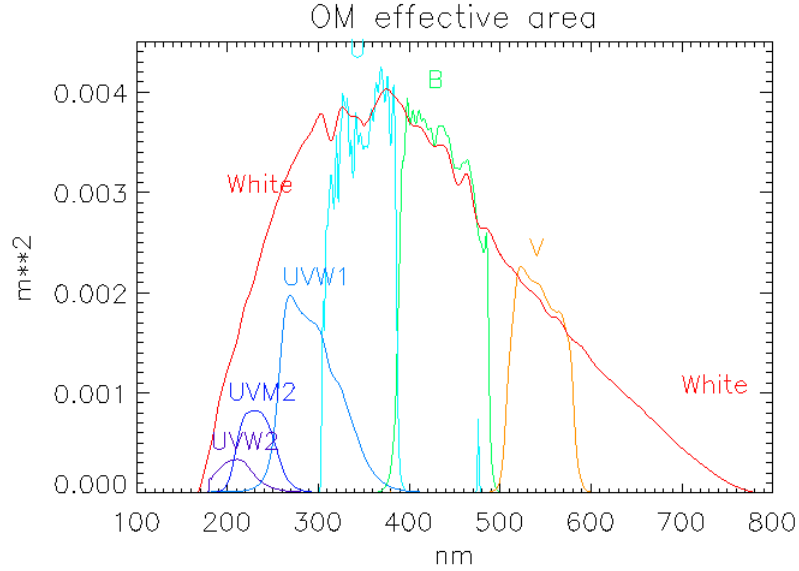


Fig. 18 The effective area curves for each of the OM photometric filters, essentially at the start of XMM-Newton mission operations (2000)

output image. These effects are generally corrected for through software tools in the XMM-Newton Science Analysis Software (SAS). Some OM observations also contain low-intensity, diffuse light features, arising from reflections from the back side of the detector entrance window and/or from a chamfer around it.

The OM, being a photon-counting instrument, has high sensitivity and, with the low background (dominated by zodiacal light), it can reach stars as faint as about $V=21$ (for a 5σ detection of an A0 star in the B filter) in 1000 s. On the other hand, the photocathode can be damaged by high incident photon rates, and this places limits on the brightest sources that the OM can be exposed to. In practice, the limiting magnitude is around $V = 7.3$ for an A0 star. A more complete description of the OM instrument is given in [8].

For observations not performed in Full-Frame mode, the OM performs a short (20 s) field-acquisition exposure at the start of each observation ([18]). This enables a number of pre-specified stars to be recognized in the exposure by the onboard software and the observed and predicted positions compared to measure shifts due to uncertainties in the spacecraft pointing. Consequently, the chosen OM science observation windows can be adjusted in position to ensure the sky coverage is optimal for the observer's science. This is especially important for accurately positioning the small Fast mode windows, when used, to ensure the target is well centered in the window.

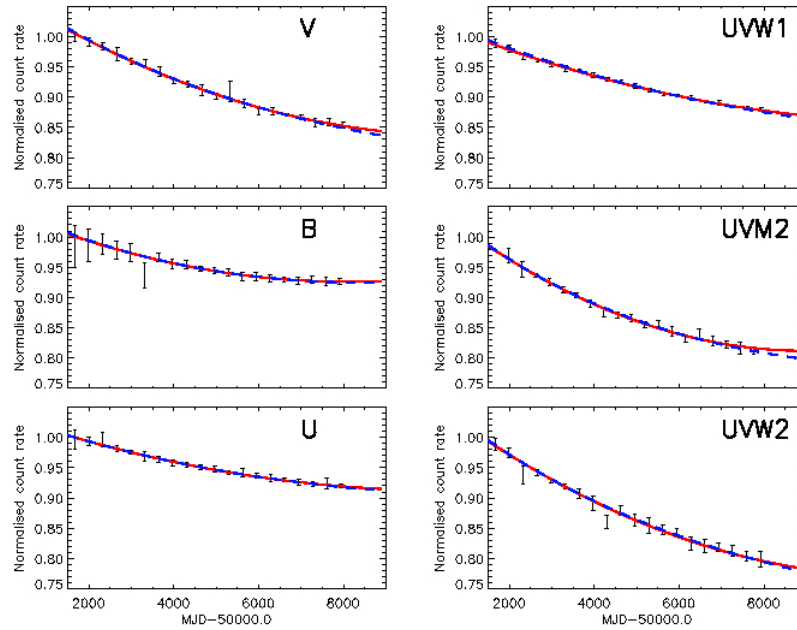


Fig. 19 Normalized, observed count rates of constant sources in the OM SUSS4 catalogue, binned into 20 time bins (black error bars), for each OM filter. The solid red and dashed blue curves represent the most recent and previously fitted decline trends, respectively, highlighting the ubiquitous flattening of the decline

In addition, the star positions are also monitored every 20 s, permitting the tracking of any spacecraft drift. This tracking information is used by the onboard software, to relocate events to the correct position in the accumulating image for Image mode data (referred to as "shift and add"). For Fast mode data, this tracking information is not applied onboard but is used for the same purpose in downstream data reduction performed by the SAS.

Scientific Performance

The OM has proven to be a very stable instrument. Nevertheless, it has experienced some spatial and temporal changes in sensitivity over the long baseline of the XMM-Newton mission, both expected and unexpected ([19]).

Of particular note are the effective areas. These were determined soon after launch, for each photometric filter, based on measurements of spectrophotometric standard stars, alongside the conversions from count rate to absolute flux and the equivalent magnitude zero-point determinations. The effective area for each filter, initially modelled from pre-launch information of the optical components (e.g., mir-

ror area, reflectivities, filter transmissions), and the quantum efficiency of the photocathode were subsequently adjusted, in-flight, to match the observed count rates of standard stars. It was found that all filters showed reduced sensitivity (from 16% to 56% residual throughput) compared to pre-launch expectations, with the UVM2 and especially UVW2 filters most affected. The reduction in sensitivity has been adequately modelled by absorption due to a molecular contaminant layer somewhere in the OM system ([20]). The effective areas of the photometric filters, essentially at launch, are shown in Fig. 18.

Subsequently, anticipated aging of the detector and, likely, some further contaminant growth have resulted in a gradual decline in sensitivity since launch. This decline, known as the time-dependent sensitivity (TDS) degradation, is filter (wavelength) dependent. It is monitored and characterized via analysis of data from the OM Serendipitous UV Sky Survey (SUSS) catalogues ([21]) and is routinely verified via observations of spectrophotometric standard stars. The most recent TDS trends for the narrowband filters are shown in Fig. 19. The decline in sensitivity ranges from around 7% in the B filter to about 22% in the UVW2 filter. These curves are used to correct the observed count rates of sources at any epoch within the mission baseline to the rate expected at the start of the mission. That rate can then be converted to absolute photometric values via the at-launch flux and zero-point conversions.

Organization of the XMM-Newton Ground Segment

The Mission Operations Centre (MOC) at the European Space Operations Centre (ESOC), Darmstadt, Germany, controls the spacecraft 24 h per day, all year round, using, as main ground stations, Kourou (French Guiana) and Sanitago (Chile) and various other additional stations in South America and Australia. The MOC is responsible for the maintenance and operations of the spacecraft and the required ground infrastructure. As XMM-Newton has no onboard data storage capacity, all data are immediately down-linked to the ground in real time. Since 2018 XMM-Newton has been operated together with Gaia and INTEGRAL.

The Science Operations Centre (SOC) at the European Space Astronomy Centre (ESAC), Villanueva de la Cañada, Madrid, Spain, is responsible for science operations and for supporting the scientific community. The SOC handles Announcements of Opportunity and proposals, including technical evaluation and OTAC support, as well as the subsequent planning of observations, including instrument handling, calibration observations, and Targets of Opportunity. Data from these observations are processed from raw telemetry to standard data products at the SOC, before being ingested into the XMM-Newton Science Archive (XSA) and distributed to the users. A Quick-Look Analysis of data and anomaly monitoring of the instruments are part of this process. The SOC also takes a leading role in the continuous calibration of the instruments and the provision of scientific analysis software (SAS) to the users together with experts from the XMM-Newton community.

The Survey Science Centre (SSC) [22], a consortium of 10 institutes in the ESA community, is responsible for the compilation of the XMM-Newton Serendipitous Source Catalogue, the follow-up/identification program for the XMM-Newton serendipitous X-ray sky survey, support to pipeline processing at the SOC, and development of parts of the scientific analysis software.

NASA provides a Guest Observer Facility (GOF) at the Goddard Space Flight Center (GSFC), Greenbelt, Maryland, USA. The GOF supports the usage of XMM-Newton by the scientific community in the USA. It distributes the XMM-Newton data to US users and contributes to the SAS development. The GOF is responsible for the organization of the Guest Observer (GO) program funded by NASA.

Observing with XMM-Newton

All the scientific instruments onboard XMM-Newton can be operated independently and can obtain science data simultaneously, if operational constraints permit. These constraints are imposed to preserve the safety of the instruments as well as to achieve the conditions for an optimal calibration of the data. The combination of the orbit of the spacecraft with limits in the instruments' operational parameters (mostly temperatures but also radiation dose) results in observation constraints related to the orientation of the spacecraft with respect to the Sun, Earth and Moon and to the position of the spacecraft in the Earth's magnetosphere.

XMM-Newton was launched in December 1999 into a highly elliptical orbit, with a high inclination with respect to the Equator and with an apogee height of 115,000 km in the Northern hemisphere and a perigee height of 6000 km in the Southern hemisphere.

Due to several perturbations, the orbit of XMM-Newton evolves with time. An orbit correction maneuver was performed in February 2003 to ensure full ground station coverage during the entire science period. But the evolution of the orbit has changed the fraction of the sky visible to science instruments and the effective available science time per orbit along the mission lifetime.

The spacecraft has no capacity for data or commanding storage onboard so it requires continuous contact with the ground for science operations. The operations are conducted from the MOC through ground stations in Kourou, Santiago de Chile and Yatharagga (and in Perth and New Norcia during the early years of the mission and occasionally in Madrid).

The EPIC and RGS CCD detectors are sensitive to both X-ray and optical radiation as well as particles. Electromagnetic radiation can affect the scientific analysis of the data collected, but protons striking the detectors can permanently damage the surface of the CCDs. In order to protect the EPIC cameras, their filter wheel is moved into the closed position during intervals of high particle radiation. The RGS spectrographs do not have a similar filter protection so the instruments are placed into a special configuration with minimal equipment switched on during high radiation intervals.

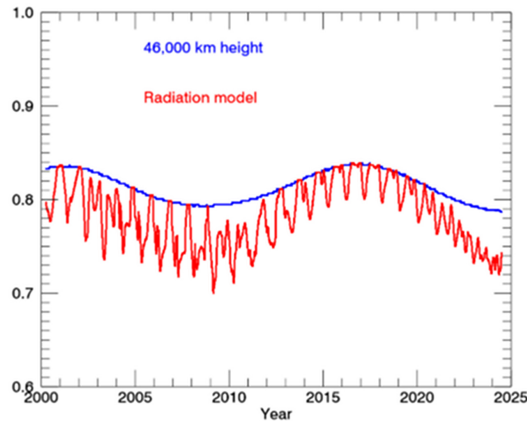


Fig. 20 The evolution of the XMM-Newton orbit during the mission has changed the spacecraft velocity near perigee passage and the orientation with respect to Earth magnetosphere. As a result the fraction of time available to science has changed with a long-term trend superposed on a seasonal modulation

Before launch, it was expected that the radiation environment above 46,000 km from the Earth was safe for the mission. This meant that ~ 143 ks of the ~ 173 ks (~ 48 h) orbital period could be devoted to science operations at the beginning of the mission. However, strong fluctuations and variability of the particle background in the cameras were one of the main surprises and concerns following launch. An ad hoc model for radiation belts around the Earth was developed in order to predict the time window within every revolution when science observations could be safely conducted [23]; see Fig. 20. According to the model and the expected orbital evolution, the science window will be as short as ~ 130 ks by 2025.

Many parameters in the EPIC cameras and RGS spectrographs are strongly dependent on the temperatures at which the instruments are operated. In order to guarantee a consistent calibration for all observations the operations are designed to maintain the temperatures of the science payload within a narrow range. Since the main source of heating is illumination by the Sun, strong constraints on temperatures are translated into a strong constraint on the orientation of the spacecraft with respect to the Sun. The solar aspect angle (angle between pointing direction and Sun direction) must be within 70° and 110° at all times to assure thermal stability and sufficient power from the solar array. This means that $\sim 65\%$ of the sky is inhibited in every single XMM-Newton revolution.

Other celestial constraints are unrelated to temperature or power stability, but to potential electromagnetic radiation damage of the OM. The main sources of dangerous light emission, away from the Sun, are the Earth and the Moon. The Earth limb avoidance angle is 42.5° , and the Moon limb avoidance angle is 22° , which is increased to 35° during eclipse seasons.

As in the case of the radiation constraints, the evolution of the XMM-Newton orbit with respect to the ecliptic has had consequences on the fraction of the sky

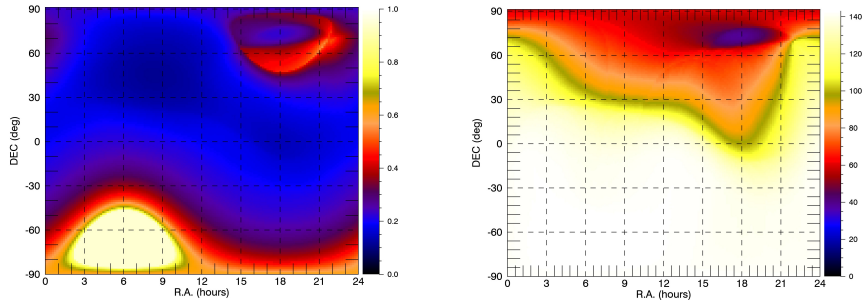


Fig. 21 The high inclination of the orbit and the high latitude of the perigee have made the South Ecliptic Pole the region of the sky with the best accessibility to XMM-Newton along its lifetime. By contrast, the visibility around the North Ecliptic Pole is constrained by the Earth in most of the revolutions. The image shows the fraction of visible orbits along 21 years (right) and the average maximum visibility in 21 year (left)

available at any time and on the evolution of the visibility in certain areas of the sky; see Fig. 21.

The constraint outlined above apply to any type of observation, independent of the configuration of the instruments. There are a number of constraints that apply only to OM exposures and some science exposures cannot be performed using the OM, but exposures with the X-ray instruments are permitted. These OM constraints refer to the presence of nearby bright celestial sources that may damage the detector. In addition, OM exposures are forbidden near the following solar system objects (Table 3):

Planet	Avoidance angle
Mars	3.5°
Jupiter	4.5°
Saturn	2°
Uranus	0.25°
Neptune	0.25°

Table 3 OM avoidance angles

Scientific Data and Analysis

XMM-Newton reformatted telemetry is organized in Observation/Slew Data Files (ODF/SDF). Most of the ODF/SDF components have a FITS format. An ASCII summary file provides the astronomers with general information on the observation and an index of the files contained in the ODF.

The Science Analysis System (SAS) is the software established to reduce and analyze XMM-Newton science data. It consists of two main blocks:

- reduction pipelines, which apply the calibrations to the ODF and the SDF science files and produce calibrated and concatenated event lists for the X-ray cameras, flat-fielded and calibrated OM sky images, source lists, and time series.
- a set of file manipulation tools, which include the extraction of spectra, light curves, and (pseudo-)images and the generation of source lists, as well as the generation of auxiliary files such as appropriate instrument response matrices.

The SAS reduction pipeline (PPS) is run on all XMM-Newton datasets. Each PPS dataset is manually screened to verify its scientific quality and identify potential processing problems. The PPS output ([24]) includes a wide range of top-level scientific products, such as X-ray camera event lists, source lists, multi-band images, background-subtracted spectra, and light curves for sufficiently bright individual sources, as well as the results of a cross-correlation with a wide sample of source catalogues and with the matching ROSAT field.

All the XMM-Newton calibration data are organized in a Current Calibration File (CCF). Summary documents, containing an overview of the current calibration status and associated systematic uncertainties, are available from the XMM-Newton Calibration Portal.

The XMM-Newton Science Archive (XSA) content is regularly updated with all the newly generated ODF, SDF, and PPS products, with updated versions of the catalogues of EPIC sources, OM sources, and Slew Survey sources, and with ancillary info like associated proposal abstract and publications. On-the-fly data analysis and processing can be performed from the XSA using the SAS without the need of downloading data or software.

With all the sources serendipitously detected in the EPIC FOV of XMM-Newton public observations, the SSC compiles and regularly updates the XMM-Newton EPIC source catalogue. At the time of writing, the SSC has created four catalogue generations, with 4XMM being the latest, with a few incremental versions for each of them, leading so far to a total of 11 catalogue data releases, 11DR. 4XMM-DR11 ([25]) was released in August 2021 and contains 787,963 “clean” detections corresponding to 602,543 unique sources covering 1239 sq. deg. In addition, the 4XMM-DR11s catalogue of serendipitous sources detected from stacked data from overlapping XMM-Newton observations ([26]) contains 358,809 unique sources of which 275,440 were multiply observed covering 350 sq. deg. The data acquired during satellite slews are used to build the XMM-Newton Slew Survey Catalogue, XMMSL2 ([27]). The current version contains 55,969 clean detections covering an area of 650,000 sq. deg. The OM team, under the auspices of the SSC, produces and regularly updates a catalogue of sources detected by the Optical Monitor. The 5th version of the XMM-Newton OM Serendipitous Ultraviolet Source Survey Catalogue, XMM-SUSS5, ([21]) contains 8,863,922 detections of 5,965,434 sources. Specific queries to all catalogues can be made using the XMM-Newton Science Archive.

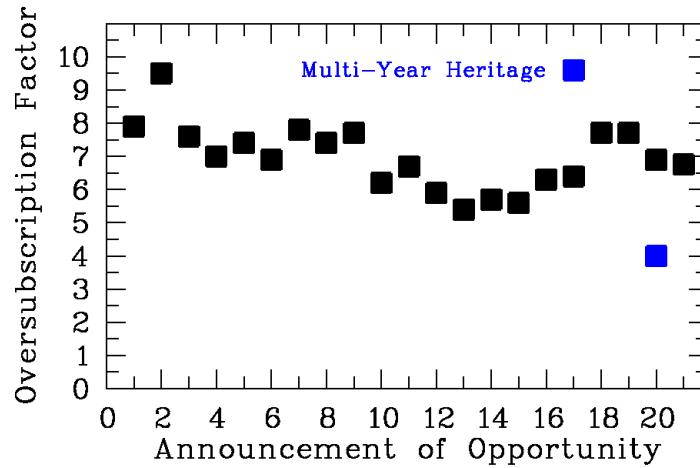


Fig. 22 The over-subscription factors, or requested versus available observing time, for the first 21 XMM-Newton Announcements of Opportunity (AOs) are shown in black. The two blue symbols show the over-subscription of the Multi-Year-Heritage programs

A database of Upper Limits across the FOV of all public XMM-Newton pointed and slew observations has been built with new observations being added as they become available ([28]). The database is searchable from the XSA interface.

Scientific Strategy and Impact

XMM-Newton observing time is made available worldwide via Announcements of Opportunity (AOs). The AOs open in the second half of August each year and the results are publicized in early December. All the AOs were highly over-subscribed, typically by a factor 6 to 7; see Fig. 22. The proposals are peer-reviewed by panels composed of scientists located worldwide.

The XMM-Newton observing strategy was discussed with the community at large at two workshops: "XMM-Newton: The next Decade" in 2007 [29] and 2016 [30] [31]. The unique capabilities of the instruments and the long mean observing time (30 ks) in combination with the possibility of long uninterrupted observations, foster XMM-Newton's potential for transformative science. Here transformative science is understood to be scientific results which lead to radically restructuring the scientific understanding or as observational confirmation of central predictions of astrophysical and cosmological theory and modelling. Examples include: (1) the non-detection or weak detection of cooling flows in the galaxy clusters Abell 1835 [32], Abell 1795 [33] and Sérsic 159-03 [34] which led to the concept of the coupling of the cosmic evolution of supermassive black holes with that of galaxies

and clusters of galaxies via feedback. This meant that two object classes which were considered to be completely independent before were from then on understood to undergo a strongly coupled evolution; (2) the detection of transitional millisecond pulsars [35], which confirmed the transition of accretion-powered to rotation-powered emission modes in pulsars; (3) the detection of low magnetic field magnetars [36] [37] which changed our understanding of the magnetic fields which cause the short X/gamma ray bursts in repeaters, (4) the identification of neutron stars within ultra-luminous X-ray sources [38] [39]. This changed the understanding of the nature of this source class and allowed the study of super-Eddington accretion [40] (5) the determination of the mass, spin and X-ray corona size of supermassive black holes [41] [42] [43] [44] [45] which quantitatively describe the inner geometry of AGNs, (6) the study of tidal disruption events [46] [47] [48] [49] [50] [51] [52] which shed light on the details of the accretion process and jet launching, (7) the detection of the warm-hot intergalactic medium [53], which confirmed cosmic simulations by the detection of the missing baryons. Further examples of transformative science resulting from XMM-Newton and Chandra observations are given in two *Nature* review articles by Santos-Leó et al. [54] and by Wilkes et al. [55].

An analysis of the science results and the discussion of the 2017 workshop showed the increased importance of Target of Opportunity observations, large and very large programs, and observations joint with other facilities for transformative science.

About 15% of submitted proposals request anticipated target of opportunity (TOO) observations. In addition there are about 45 requests for unanticipated TOOs and/or Director's discretionary time observations each year, which in general are forwarded to an OTAC (Observing Time Allocation Committee) chairperson for a recommendation. XMM-Newton has not formally limited the time available for TOOs. However, the high amount of fixed-time observations and observations performed simultaneously with other missions limit the time which may be allocated to TOO observations. In the very late 2010s and very early 2020s XMM-Newton typically performed 80 TOO observations per year. This rate is more than double the rate of TOO observations in the early days of the mission (e.g., 2005); see Fig. 23 and Fig. 25.

Multi-wavelength and multi-messenger observations are a powerful tool to foster transformative science. With its suite of instruments, XMM-Newton already provides multi-wavelength coverage from the optical to X-ray regimes. XMM-Newton SOC staff investigated ways to further extend this approach to "multi"-wavelength observations. These can be performed via joint programs. In 2021, XMM-Newton has joint programs with nine facilities. The joint programs allow the time allocation committees of each facility to allocate time on the other mission in connection with the allocation of time on the own facility. Therefore, with one proposal, in response to an XMM-Newton AO, observing time on up to 10 facilities can be requested. Table 4 shows the joint programs and the time exchanged per year. The XMM-Newton joint programs allow the spectral energy distribution of a source to be covered from the radio, optical, UV and X-ray, Γ -ray all the way to the TeV range. About 30% of the performed high-priority observations (i.e. observations whose execution is

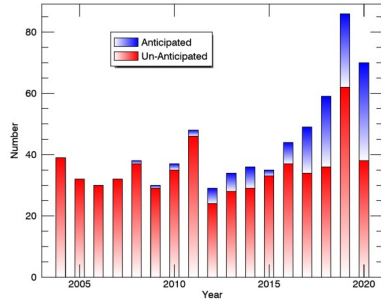


Fig. 23 Performed Target of Opportunity observations

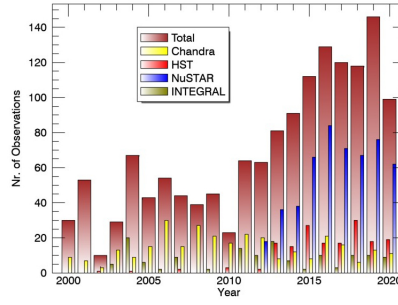


Fig. 24 Observations performed coordinated or simultaneous with other facilities

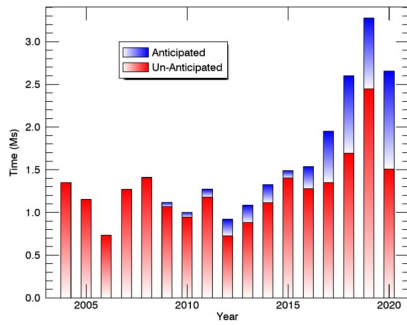


Fig. 25 Observing time performed for Target of Opportunity observations

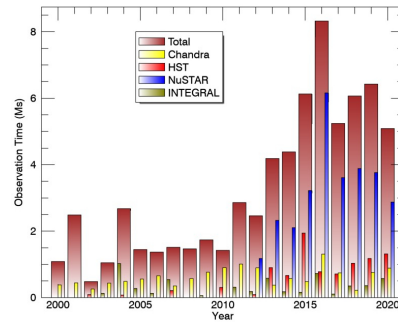


Fig. 26 Observing time performed coordinated or simultaneous with other facilities

guaranteed) are from a joint program, most of them simultaneous with one or more facilities; see Fig. 24 and Fig. 26.

Facility	Exchanged time
NRAO	2×150 ks
VLT(I)	2×290 ks
HST	2×150
Chandra	2×1 Ms
Swift	300 ks
NuSTAR	2×1.5 Ms
INTEGRAL	2×300 ks
MAGIC	2×150 ks
H.E.S.S.	2×150 ks

Table 4 Joint Programmes.

Requests for observing time longer than 300 ks are submitted as large programs. About 40% of the high-priority observing time (execution guaranteed) is given to large programs, such that they have the same over-subscription as the normal pro-

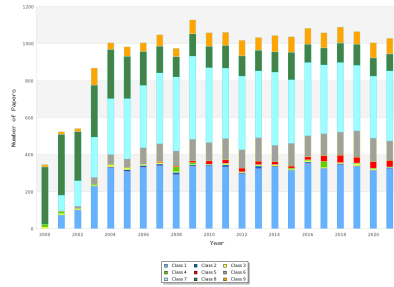


Fig. 27 Classification of all refereed articles listed in ADS which contain "XMM" in a full text-search: (1) article makes use of XMM-Newton data or pipeline products; (2) catalogue based on XMM-Newton observations; (3) article makes quantitative predictions for XMM-Newton observations; (4) article describes XMM-Newton, its instruments, scientific impact, etc. (5) article makes use of the primary catalogues (6) article makes use of published XMM-Newton results (7) article refers to papers presenting XMM-Newton results (8) article refers to "XMM-Newton" in general (9) article uses expression derived from XMM-Newton, e.g., names of objects

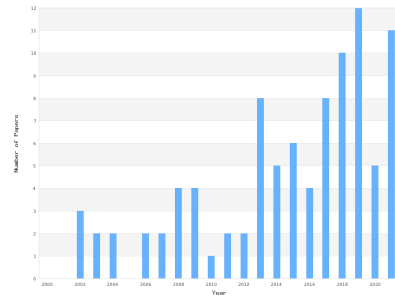


Fig. 28 Articles in *Nature* and *Science* making use of XMM-Newton data are shown per year as an indicator of the amount of transformative science results

grams. Examples of transforming science resulting from larger programs are given in [41], [44], [53] To accomplish programmes requiring more than 2 Ms, e.g., [56], the call for Multi-Year-Heritage (MYH) program was introduced in 2017. Here, up to 6 Ms of observing time are available for distribution, to be executed over a period of three AOs (3 years). The call for MYH programs in 2017 had an over-subscription of a factor 10. The call in 2020 suffered the pandemic constraints showing a lower over-subscription.

The distribution of elapsed time between performed observations and publication peaks at 2 years [57]. Most of the times, TOO observations lead to rapid publications with about 1 year elapsed time between observation and publication [57]. The predefined observing modes in combination with the provided support, e.g., pipeline products, calibration, archive, or catalogues, make XMM-Newton data highly comparable and therefore ideally suited for studies based on archival data. In fact 90% of the observing time has been used in at least one publication [57].

XMM-Newton data also play an important role in education and in the development of new generations of researchers around the world. At the time of writing (November 2021), 406 Ph.D. theses had used XMM-Newton data or included results of research related to the development of the instruments. XMM-Newton is frequently used by young scientists who are starting their career in astrophysics. Since the 5th call for observing time proposals, in 2005, astronomers sending proposals the first time submit about 20% of the proposals of each call. The success

rate of these first-time proposers is slightly below the average success rate of all proposers. Remarkably, in more than one third of the calls since 2005, the rate of requested to allocated observing time secured by first-time proposers was similar or even larger than the average rate of all proposers.

About 380 articles are published in refereed journals each year making use of XMM-Newton data, describing the instruments, or using pipeline products or the catalogue. Figure 27 gives an analysis of all refereed articles listed in ADS, which mention XMM-Newton, demonstrating not only the usage of XMM-Newton data but also its impact via citations. Articles containing results based on XMM-Newton observations are about three times more cited than all astronomical papers. Fig. 28 shows the number of articles making use of XMM-Newton data published in *Nature* or *Science* journal demonstrating the high amount of transforming science which typically is published in these two journals.

Authors Contribution

Norbert Schartel and Maria Santos-Lleó contributed the "Introduction", "Scientific Data and Analysis", and "Scientific Strategy and Impact" sections, Rosario González-Riestra contributed "The Reflection Grating Spectrometers (RGSs)" section, Peter Kretschmar contributed the "Organization of the XMM-Newton Ground Segment" section, Marcus Kirsch contributed "The Spacecraft" section, Pedro Rodríguez contributed the "Observing with XMM-Newton" section, Simon Rosen contributed the "Optical Monitor (OM)" section, Michael Smith and Martin Stuhlinger contributed the "European Photon Imaging Camera (EPIC)" section and Eva Verdugo-Rodrigo contributed the "X-ray Mirrors" section. Norbert Schartel prepared the chapter outline compiled and homogenized the different contributions.

Acknowledgments

The authors deeply thank Arvind Parmar for many useful suggestions and Lucia Ballo for help with the statistical numbers for joint programs. The authors also acknowledge the outstanding contribution of the Survey Science Centre to the mission success and the dedication and excellence of the rest of the team members of the XMM-Newton Mission Operations and Science Operations centres, where the authors of this paper feel as an honour to serve.

References

- [1] Jansen F, Lumb D, Altieri B et al (2001) XMM-Newton observatory - I. The spacecraft and operations. *A&A* 365:L1-L6
- [2] Trümper J (1982) The ROSAT mission. *Adv. Space Res.* 2:241-249
- [3] Boella G, Butler RC, Perola GC et al (1997) BeppoSAX, the wide band mission for X-ray astronomy. *A&AS* 122:299-307
- [4] Longdon N, Melita G (1985) An ESA Workshop on a Cosmic X-ray Spectroscopy Mission. ISSN 0379-6566, SP-239, ESA Publications Division, Noordwijk, The Netherlands
- [5] den Herder J W, Brinkman A C, Kahn S M et al (2001) The Reflection Grating Spectrometer on board XMM-Newton. *A&A*, 365, L7-L17
- [6] Turner M J L, Abbey A, Arnaud M et al (2001) The European Photon Imaging Camera on XMM-Newton: The MOS cameras. *A&A*, 365, L27-L35
- [7] Strüder L, Briel U, Dennerl K et al (2001) The European Photon Imaging Camera on XMM-Newton: The pn-CCD camera. *A&A*, 365, L18-L26
- [8] Mason, K O, Breeveld A A, Much R et al (2001) The XMM-Newton optical/UV monitor telescope. *A&A* 365:L36-L44
- [9] Kirsch M G F et al (2010) XMM-Newton, ESAs X-ray observatory, the Loss of Contact Rescue and Mission Operations ready for the next decade. *American Institute of Aeronautics and Astronautics* 2010: 2123
- [10] Pantaleoni M et al (2012) XMM-Newton's operational challenge of changing the attitude control to 4 active reaction wheels, after 12 years of routine operations. *American Institute of Aeronautics and Astronautics*, AIAA 2012:1275587
- [11] Kirsch M G F et al (2014) Extending the lifetime of ESA's X-ray observatory XMM-Newton. *American Institute of Aeronautics and Astronautics* 2014:1608
- [12] Gondoin P, Aschenbach B R, Beijersbergen M W et al (1998) Calibration of the XMM Flight Modules - Image quality. *SPIE Vol. 3444:278-289*
- [13] Gondoin P, Aschenbach B R, Beijersbergen M W et al (1998) Calibration of the first XMM flight mirror module: II. Effective area. *SPIE Vol. 3444:290-301*
- [14] Aschenbach B (2002) In-orbit performance of the XMM-Newton x-ray telescopes: images and spectra. *SPIE Vol. 4496:8-22*,
- [15] Ebrero J (2021) XMM-Newton Users Handbook, Issue 2.19. https://xmm-tools.cosmos.esa.int/external/xmm_user_support/documentation/uhb/
- [16] de Vries C P, den Herder J W, Gabriele, C, et al (2015) Calibration and in-orbit performance of the reflection grating spectrometer onboard XMM-Newton. *Astronomy and Astrophysics* 573: 128–156
- [17] González-Riestra R. Status of the RGS Calibration (2021). <https://xmmweb.esac.esa.int/docs/documents/CAL-TN-0030.pdf>

- [18] Talavera, A. & Rodriguez, P. (2011) Astrometry with the Optical Monitor on board XMM-Newton: OM Field Acquisition and SAS: variable boresight. <https://xmmweb.esac.esa.int/CoCo/CCB/DOC/Attachments/INST-TN-0041-1-0.pdf>
- [19] Rosen, S. (2020) XMM-Newton Optical and UV Monitor (OM) Calibration Status. <https://xmmweb.esac.esa.int/docs/documents/CAL-TN-0019.pdf>
- [20] Kirsch M G F, Abbey A, Altieri B et al (2005) Health and cleanliness of the XMM-Newton science payload since launch. SPIE, 5898:224-235
- [21] Page M J, Brindle C, Talavera A et al (2012) The XMM-Newton serendipitous ultraviolet source survey catalogue MNRAS, 426:903-926
- [22] Watson M G, Auguères J L, Ballet J et al (2001) The XMM-Newton Serendipitous Survey - I. The role of XMM-Newton Survey Science Centre. A&A 365:L51-L59
- [23] Casale, M. & Fauste, J. (2004) Attempt of modelling the XMM-Newton radiation environment. http://xmmweb.esac.esa.int/external/xmm_sched/vischeck/Rad_Model_TN.pdf
- [24] Rodríguez P (2021) Specifications for Individual SSC Data Products <https://xmmweb.esac.esa.int/docs/documents/XMM-SOC-GEN-ICD-0024.pdf>
- [25] Webb, N. A., Coriat, M., Traulsen, I. et al (2020) The XMM-Newton serendipitous survey. IX. The fourth XMM-Newton serendipitous source catalogue. A&A 641: A136
- [26] Traulsen I, Schwöpe, A. D.; Lamer, G. et al (2020) The XMM-Newton serendipitous survey. X. The second source catalogue from overlapping XMM-Newton observations and its long-term variable content. A&A 641:A137
- [27] Saxton R D., Read A M, Esquej P et al (2008) The first XMM-Newton slew survey catalogue: XMMSL1. A&A 480:611-622
- [28] Ruiz, A., Georgakakis, A., Gerakakis, S. et al (2021) The RapidXMM Upper Limit Server: X-ray aperture photometry of the XMM-Newton archival observations. [arXiv:2106.01687v1](https://arxiv.org/abs/2106.01687v1)
- [29] Schartel N (2008) XMM-Newton: The next decade. *Astronomische Nachrichten* 329, Issue 2:111-113
- [30] Schartel N (2017) Editor's note. *Astronomische Nachrichten* 388: 139
- [31] Schartel N, Jansen F, Ward M J (2017) XMM-Newton: Status and scientific perspective. *Astronomische Nachrichten* 388: 354-359
- [32] Peterson J R, Paerels F B S, Kaastra J S et al (2001) X-ray imaging-spectroscopy of Abell 1835. *Astronomy and Astrophysics* 365:L104-L109
- [33] Tamura T., Kaastra J S, Peterson J R et al (2001) X-ray spectroscopy of the cluster of galaxies Abell 1795 with XMM-Newton. *Astronomy and Astrophysics* 365:L87-L92
- [34] Kaastra J S, Ferrigno C, Tamura T (2001) XMM-Newton observations of the cluster of galaxies Sérsic 159-03. *Astronomy and Astrophysics* 365:L99-L103

- [35] Papitto A., Ferrigno C, Bozzo E et al (2013) Swings between rotation and accretion power in a binary millisecond pulsar. *Nature* 501:517-520
- [36] Rea N., Esposito P, Turolla R et al (2010) A Low-Magnetic-Field Soft Gamma Repeater *Science* 330:944-946
- [37] Tiengo A, Esposito P, Mereghetti S et al. (2013) A variable absorption feature in the X-ray spectrum of a magnetar. *Nature* 500:312-314
- [38] Fürst F, Walton D J, Harrison F A et al (2016) Discovery of Coherent Pulsations from the Ultraluminous X-Ray Source NGC 7793 P13 *The Astrophysical Journal Letters* 831:L14
- [39] Israel G L, Belfiore A, Stella L et al (2017) An accreting pulsar with extreme properties drives an ultraluminous x-ray source in NGC 5907. *Science* 355:817-819
- [40] Pinto Ciro, Middleton M J, Fabian A C (2016) Resolved atomic lines reveal outflows in two ultraluminous X-ray sources. *Nature* 533:64-67
- [41] Fabian A C, Zoghbi A, Ross R R et al (2009) Broad line emission from iron K- and L-shell transitions in the active galaxy 1H0707-495 *Nature* 459:540-542
- [42] Risaliti G, Harrison F A, Madsen K K et al (2013) A rapidly spinning supermassive black hole at the centre of NGC 1365. *Nature* 494:449-451
- [43] Parker M L., Pinto C, Fabian A C et al (2017) The response of relativistic outflowing gas to the inner accretion disk of a black hole. *Nature* 543:83-86
- [44] Alston W N, Fabian A C, Kara E (2020) A dynamic black hole corona in an active galaxy through X-ray reverberation mapping. *Nature Astronomy* 4:597-602
- [45] Wilkins D R, Gallo L C, Costantini E et al (2021) Light bending and X-ray echoes from behind a supermassive black hole. *Nature* 595:657-660
- [46] Reis R C, Miller J M, Reynolds MT et al (2012) A 200-Second Quasi-Periodicity After the Tidal Disruption of a Star by a Dormant Black Hole *Science* 337:949-951
- [47] Miller J M, Kaastra J S, Miller M C et al (2015) Flows of X-ray gas reveal the disruption of a star by a massive black hole. *Nature* 526: 542-545
- [48] Kara E, Miller Jon M, Reynolds C et al (2016) Relativistic reverberation in the accretion flow of a tidal disruption event. *Nature* 535:388-390
- [49] Lin D, Guillochon J, Komossa S et al (2017) A likely decade-long sustained tidal disruption event *Nature Astronomy* 1:33
- [50] Lin D, Strader J, Carrasco E R et al (2018) A luminous X-ray outburst from an intermediate-mass black hole in an off-centre star cluster *Nature Astronomy* 2:656-661
- [51] Pasham D R, Remillard R A, Fragile P C et al (2019) A loud quasi-periodic oscillation after a star is disrupted by a massive black hole. *Science* 363:531-534
- [52] Shu X, Zhang W, Li S et al (2020) X-ray flares from the stellar tidal disruption by a candidate supermassive black hole binary *Nature Communications* 11: article id. 5876
- [53] Nicastro, F.; Kaastra, J.; Krongold, Y. et al (2018) Observations of the missing baryons in the warm-hot intergalactic medium *Nature* 558:406-409

- [54] Santos-Lleo M, Schartel N, Tananbaum H et al (2009) The first decade of science with Chandra and XMM-Newton. *Nature* 462:997-1004
- [55] Wilkes B, Tucker W, Santos-Lleo M et al (2022) X-ray astronomy comes of age. *Nature* 606:261-271
- [56] Pierre M, Adami C, Birkinshaw M et al (2017) The XXL survey: First results and future. *Astronomische Nachrichten* 338, Issue 334:334-341
- [57] Ness J U, Parmar A N, Valencic L A et al (2014) XMM-Newton publication statistics. *Astronomische Nachrichten* 335, Issue 2:210-220